We are IntechOpen, the world's leading publisher of Open Access books Built by scientists, for scientists

6,900
Open access books available

185,000
International authors and editors

200M
Downloads

Our authors are among the

154
Countries delivered to

TOP 1%
most cited scientists

12.2%
Contributors from top 500 universities



WEB OF SCIENCE™

Selection of our books indexed in the Book Citation Index in Web of Science™ Core Collection (BKCI)

Interested in publishing with us?
Contact book.department@intechopen.com

Numbers displayed above are based on latest data collected.
For more information visit www.intechopen.com



8

Barotropic Aspects of Hurricane Structural and Intensity Variability

Eric A. Hendricks[1], Hung-Chi Kuo[2], Melinda S. Peng[3] and Daniel Hodyss[4]
[1,3,4]*Marine Meteorology Division, Naval Research Laboratory, Monterey, CA*
[2]*National Taiwan University, Taipei*
[1,3,4]*USA*
[2]*Taiwan*

1. Introduction

Hurricanes are intense atmospheric vortices characterized by extreme winds, torrential rain, and destructive storm surges. When a major hurricane makes landfall one or more of these processes can cause immense property damage and loss of life. Considerable progress has been made in recent decades unlocking the physical and dynamical mechanisms by which hurricanes form, and by which they change their structure and intensity. In spite of this progress, intensity forecast skill has shown little to no improvement in the past twenty years. During this same time period, global numerical weather prediction models have steadily improved in their ability to predict the large-scale environment. However, better knowledge of the environment has not led to significant intensity forecast skill improvements. The reason for this is that hurricane intensity and structure change is controlled to a large degree by internal dynamical processes, which are less well understood and predictable. Although these internal processes interact with the large-scale environment in complicated ways, much insight can first be obtained by examining these processes in the absence of environmental and ocean surface forcing, and in a two-dimensional framework.

We define internal dynamical processes here as those processes that occur within the region defined by twice the radius of maximum wind, or typically within approximately 150 km of the center of the hurricane, and whose dynamics is constrained to the hurricane vortex itself and not the environment. The internal processes of principle importance for the evolution of the hurricane vortex are the formation and evolution of spiral rainbands, mixing between the eye and eyewall, and concentric eyewall cycles. While in the real atmosphere, these processes are inherently three-dimensional and influenced by moist processes and friction, much insight into the dynamics can first be obtained in a simpler unforced barotropic framework. Strictly speaking, *barotropic* means that atmopheric pressure depends only on density, while *baroclinic* means that pressure depends both on density and temperature. Since tropical cyclones are surface based vortices whose winds decay with increasing height, the vertical shear of the vortex tangential winds are balanced by radial temperature gradients, making it baroclinic and giving it a warm-core signature at upper levels. However, if one is considering the behavior of a tropical cyclonce (hereafter TC) at lower levels where the vortex tangential winds are not changing significantly with height, a barotropic model is a good starting point.

The outline of this chapter is as follows. In section 2, we present the dynamical model used for this study, as well the fundamental principles associated with it. In section 3, the dynamical model and observations are used to examine barotropic aspects of inner and outer spiral rainbands, instabilities and mixing processes between the eye and eyewall, and concentric eyewall cycles. A summary of the results is given in section 4.

2. Dynamical model and fundamentals

2.1 Divergent barotropic model

Our dynamical model here is the divergent barotropic (or shallow water) equations on an f-plane in polar coordinates (r,ϕ,t), where r is the radius from the origin, ϕ is the azimuthal angle, and t is the time. The equations governing radial momentum u and tangential momentum v are

$$\frac{Du}{Dt} - fv - \frac{v^2}{r} + g\frac{\partial h}{\partial r} = 0, \tag{1}$$

$$\frac{Dv}{Dt} + fu + \frac{uv}{r} + g\frac{\partial h}{r\partial \phi} = 0, \tag{2}$$

where $D/Dt = \partial/\partial t + u\partial/\partial r + (v/r)\partial/\partial\phi$ is the material derivative. Equations (1) and (2) indicate that in a Lagrangian reference frame, an air parcel may be accelerated by the Coriolis, centrifugal, and pressure gradient forces, respectively. By taking the curl and divergence of equations (1) and (2), the equations governing the relative vorticity $\zeta = \partial(rv)/r\partial r - \partial u/r\partial\phi$ and divergence $\delta = \partial(ru)/r\partial r + \partial v/r\partial\phi$ are

$$\frac{\partial \zeta}{\partial t} + \frac{\partial[r(f+\zeta)u]}{r\partial r} + \frac{\partial[(f+\zeta)v]}{r\partial\phi} = 0, \tag{3}$$

$$\frac{\partial \delta}{\partial t} - \frac{\partial[r(f+\zeta)v]}{r\partial r} + \frac{\partial[(f+\zeta)u]}{r\partial\phi} + \nabla^2\left[gh + \tfrac{1}{2}\left(u^2+v^2\right)\right] = 0. \tag{4}$$

The conservation of mass is

$$\frac{\partial h}{\partial t} + \frac{\partial(rhu)}{r\partial r} + \frac{\partial(hv)}{r\partial\phi} = 0, \tag{5}$$

where h is the fluid depth. It is convenient to express u, v, ζ, δ in terms of the velocity potential χ and the streamfunction ψ as

$$u = \frac{\partial\chi}{\partial r} - \frac{\partial\psi}{r\partial\phi}, \qquad v = \frac{\partial\chi}{r\partial\phi} + \frac{\partial\psi}{\partial r}, \tag{6}$$

$$\zeta = \nabla^2\psi, \qquad \delta = \nabla^2\chi, \tag{7}$$

where $\nabla^2 = (\partial/r\partial r)(r\partial/\partial r) + \partial^2/r^2\partial^2\phi$. By combining (3) and (5) while eliminating the divergence, the potential vorticity principle is obtained:

$$\frac{DP}{Dt} = 0, \tag{8}$$

where $P = (f+\zeta)/h$ is the potential vorticity. Equation (8) indicates that for shallow water motions in the absence of friction, individual fluid parcels conserve their PV as they are advected in the flow.

2.2 Diagnostic balance equation

By setting $\partial\delta/\partial t = 0$ in (4), and neglecting terms involving the velocity potential χ, the relationship

$$f\nabla^2\psi + 2\left[\frac{\partial^2\psi}{\partial r^2}\left(\frac{1}{r^2}\frac{\partial^2\psi}{\partial\phi^2}+\frac{1}{r}\frac{\partial\psi}{\partial r}\right)-\left(\frac{1}{r}\frac{\partial^2\psi}{\partial r\partial\phi}-\frac{1}{r^2}\frac{\partial\psi}{\partial\phi}\right)^2\right] = g\nabla^2 h \tag{9}$$

between ψ and h is obtained. This is the *nonlinear balance equation* in polar coordinates. Equation (9) indicates that given ψ or h with appropriate boundary conditions, the other field which is in quasi-balance with that field may be obtained. Since $P = (\nabla^2\psi + f)/h$, equations (8) and (9) are sufficient to describe the quasi-balanced evolution of a shallow water vortex. By substituting $h = (\nabla^2\psi + f)/P$ into the right hand side of (9), an invertibility relationship is obtained, where ψ, h, ζ, u and v may be obtained diagnostically, given P. This invertibility principle is the reason P is such a useful dynamical quantity. The shallow water dynamics can be succintly speficied by one prognostic PV equation and a diagnostic relationship for the other quasi-balanced fields. For the special case of axisymmetric flow in which $v = \partial\psi/\partial r$ and $u = -\partial\psi/r\partial\phi = 0$, equation (9) reduces to

$$\frac{\partial}{r\partial r}\left[r\left(fv+\frac{v^2}{r}-g\frac{\partial h}{\partial r}\right)\right] = 0, \tag{10}$$

implying that, when enforcing the boundary conditions,

$$fv+\frac{v^2}{r}-g\frac{\partial h}{\partial r} = 0, \tag{11}$$

which is the gradient wind balance equation. In this context, (9) is a more general formulation of the gradient wind balance equation when the flow is both asymmetric and balanced.

2.3 Linearization

Equations (3)-(5) cannot be solved analytically due to the nonlinear terms. However, under the assumption that perturbations are small in comparison to their means, a modified set of equations can be obtained that can be solved analytically. This process is referred to as *linearization*. In order to linearize (3)-(5), a basic state chosen here is that of an arbitrary axisymmetric vortex $\bar{\omega}(r) = \bar{v}(r)/r$ that is in gradient balance with the height $\bar{h}(r)$. While our basic state vortex is prescribed to be axisymmetric, the basic state could similarly be obtained by taking an azimuthal mean, i.e.,

$$\bar{v}(r) = \frac{1}{2\pi}\int_0^{2\pi} v(r,\phi)\,d\phi, \tag{12}$$

and similar definitions hold for the other variables. The decomposition for all variables is as follows: $h(r) = \bar{h}(r) + h'(r,\phi,t)$, $v(r) = \bar{v}(r) + v'(r,\phi,t)$, $u(r) = u'(r,\phi,t)$, $\zeta(r) = \bar{\zeta}(r) + \zeta'(r,\phi,t)$, $\delta(r) = \delta'(r,\phi,t)$, $\chi(r,\phi,t) = \chi'(r,\phi,t)$, and $\psi(r,\phi,t) = \psi'(r,\phi,t)$. The perturbations u', v', ζ', and δ' are related to ψ' and χ' as above. Upon substituting the decomposed variables into (3)-(5), enforcing the gradient balance constraint, and neglecting higher order terms involving multiplication of perturbation quantities, we obtain the linearized versions of (3)-(5) which govern small amplitude disturbances about the basic state vortex,

$$\left(\frac{\partial}{\partial t}+\bar{\omega}\frac{\partial}{\partial\phi}\right)\nabla^2\psi' + \bar{\eta}\nabla^2\chi' + \left(\frac{\partial\chi'}{\partial r}-\frac{\partial\psi'}{r\partial\phi}\right)\frac{d\bar{\zeta}}{dr} = 0, \tag{13}$$

$$\left(\frac{\partial}{\partial t}+\bar{\omega}\frac{\partial}{\partial \phi}\right)\nabla^2\chi' - \bar{\eta}\nabla^2\psi' + g\nabla^2 h' - \left(\frac{\partial \chi'}{r\partial \phi}+\frac{\partial \psi'}{\partial r}\right)\frac{d\bar{\zeta}}{dr}=0, \tag{14}$$

$$\left(\frac{\partial}{\partial t}+\bar{\omega}\frac{\partial}{\partial \phi}\right)h' + \bar{h}\nabla^2\chi' + \left(\frac{\partial \chi'}{\partial r}-\frac{\partial \psi'}{r\partial \phi}\right)\frac{d\bar{h}}{dr}=0, \tag{15}$$

where $\bar{\eta} = f + \bar{\zeta}$ is the basic state absolute vertical vorticity. We wish to understand the nature and behavior of small disturbances (i.e., waves) on this basic state vortex. Using the Wentzel-Kramers-Brillouin (WKB) approximation, we assume normal mode solutions of the form $\psi'(r,\phi,t) = \hat{\psi}\exp[i(kr+m\phi-\nu t)]$, $\chi'(r,\phi,t) = \hat{\chi}\exp[i(kr+m\phi-\nu t)]$, and $h'(r,\phi,t) = \hat{h}\exp[i(kr+m\phi-\nu t)]$, where k is the radial wavenumber (i.e., the number of wave crests per unit radial distance), m is the azimuthal wave number (i.e., the number of wave crests per 2π radians), ν is the complex frequency, and $\hat{\psi}$, $\hat{\chi}$, and $\hat{h}$ are complex constants. Substituting the assumed solution into (13)-(15), we obtain a matrix eigenvalue problem $\mathbf{Ax} = \mathrm{i}(\nu - \bar{\omega}m)\mathbf{Ix}$, where $\mathbf{x} = (\psi', \chi', h')$ and $\mathbf{I}$ is the identity matrix, for the Doppler-shifted frequency $\nu - \bar{\omega}m$. The Doppler-shifted frequency is the frequency of the wave perceived by an observer moving with the hurricane flow, and is always lower than the actual frequency of the wave for positive $\bar{\omega}$. This eigenvalue problem can be written as $\mathbf{Bx} = 0$. By setting the determinant of $\mathbf{B}$ equal to zero, two cubic equations can be obtained that can be solved for the real and imaginary portions (ν_r and ν_i) of the complex Doppler-shifted frequency $\nu = \nu_r + i\nu_i - \bar{\omega}m$. The real portion encapsulates lower frequency vortex Rossby waves, higher frequency inertia-gravity waves, and mixed inertia-gravity-vortex Rossby waves (with inseparable dispersion characteristics) and when combined with a nonzero imaginary portion, exponentially growing and decaying modes exist - the former of which is the Rossby-inertia gravity wave instability (Ford, 1994; Schecter & Montgomery, 2004; Hodyss & Nolan, 2008; Hendricks et al., 2010). It is not our intent in here to describe this more complex dispersion relationship, but rather to isolate the primary modes of variability on shallow water vortices by making certain simplifying assumptions on (13)-(15), foremost of which is neglecting the unstable modes. The local dispersion relationship for the inward and outer propagating inertia-gravity waves can be found by setting $d\bar{\zeta}/dr = d\bar{h}/dr = 0$ in equations (13)-(15) and assuming a constant rotation rate $\bar{\omega}$, yielding

$$(\nu - \bar{\omega}m)^2 = (f+2\bar{\omega})^2 + g\bar{h}\left(k^2 + m^2/r^2\right). \tag{16}$$

The local radial $c_r = \nu/k$ and azimuthal $c_\phi = r\nu/m$ phase velocites are then

$$c_r = \frac{\bar{\omega}m}{k} \pm \frac{1}{k}\left[(f+2\bar{\omega})^2 + g\bar{h}\left(k^2+m^2/r^2\right)\right]^{1/2}, \tag{17}$$

$$c_\phi = \bar{v}(r) \pm \frac{r}{m}\left[(f+2\bar{\omega})^2 + g\bar{h}\left(k^2+m^2/r^2\right)\right]^{1/2}. \tag{18}$$

Note that inertia-gravity waves may propagate both radially outward and inward, and azimuthally prograde and retrograde. Similarly, in the nondivergent limit of (13)-(15) (i.e., $\chi' = 0$ and $h' = 0$) we obtain the vortex Rossby wave dispersion relationship obtained by Montgomery & Kallenbach (1997)

$$\nu - \bar{\omega}m = \frac{m}{r}\frac{d\bar{\zeta}/dr}{k^2+m^2/r^2}. \tag{19}$$

Note that the Doppler-shifted frequency is directly proportial to the basic state vorticity gradient $d\bar{\zeta}/dr$, and inversely proportial to the square of the total wavenumber $k^2 + m^2/r^2$. The local radial and azimuthal phase velocities for vortex Rossby waves are

$$c_r = \frac{\bar{\omega} m}{k} + \frac{m}{kr} \frac{d\bar{\zeta}/dr}{k^2 + m^2/r^2}, \tag{20}$$

$$c_\phi = \bar{v}(r) + \frac{d\bar{\zeta}/dr}{k^2 + m^2/r^2}. \tag{21}$$

As shown by equations (20) and (21), vortex Rossby waves may propagate both radially inward and outward, and azimuthally prograde and retrograde with respect to the local flow, depending on the sign of $d\bar{\zeta}/dr$. For a shallow water vortex with monotonically decreasing basic state vorticity, vortex Rossby waves propagate azimuthally slower than the local flow. Therefore, they are analogous to planetary Rossby waves, with $d\bar{\zeta}/dr$ being the local beta effect. The radial group velocity for vortex Rossby waves is

$$\frac{\partial \nu}{\partial k} = c_{gr} = \frac{-2km}{r} \frac{d\bar{\zeta}/dr}{(k^2 + m^2/r^2)^2}. \tag{22}$$

Equation (22) indicates that the energy from a vortex Rossby wave packet is directed radially outward for $d\bar{\zeta}/dr < 0$ (e.g., a monotonic vortex as above) and radially inward for $d\bar{\zeta}/dr > 0$. For this reason, vortex Rossby waves that are excited locally can affect the vortex in regions away from the location of wave excitation through wave-mean flow interaction. According to the radial phase velocity equation, as the radial wavenumber k increases, the radial phase velocity approaches zero. Since the anticyclonic shear outside the radius of maximum wind in hurricanes has a symmetrizing affect on disturbances (increasing the radial wavenumber), this implies a stagnation radius where the wave can no longer propagate radial outward. In this regard, vortex Rossby waves are quite different from inertia-gravity waves since they cannot radiate outward to infinity. As we will see in section 3, for this reason only inner spiral rainbands can be described by vorted Rossby wave theory, since the outer bands exist in regions of approximately zero basic state PV gradient.

Dispersion curves are plotted for the all three wave types in Figure 1. It is readily apparent that vortex Rossby waves and inertia-gravity waves have very different dispersion characteristics. In particular, the frequencies of the outward and inward propagating inertia-gravity waves increase with increasing radial wavenumber, while for vortex Rossby waves the frequency approaches zero with increasing radial wavenumber. For vortex Rossby waves, the frequency always has the same sign as $d\bar{\zeta}/dr$, resulting in waves that propagate to the local *west* of the radial basic state vorticity gradient. Additionally the absolute value of the frequency is larger for lower azimuthal wavenumbers than for higher azimuthal wavenumbers. When $d\bar{\zeta}/dr < 0$, this indicates that absolute phase speeds for those waves are smallest.

2.4 Energy and angular momentum principles

The energy principle associate with (1),(2) and (5) can be derived by first rewriting (1)-(2) in their rotational forms as

$$\frac{\partial u}{\partial t} - hPv + \frac{\partial}{\partial r}\left[gh + \tfrac{1}{2}(u^2 + v^2)\right] = 0, \tag{23}$$

$$\frac{\partial v}{\partial t} + hPu + \frac{\partial}{r\partial \phi}\left[gh + \tfrac{1}{2}(u^2 + v^2)\right] = 0. \tag{24}$$

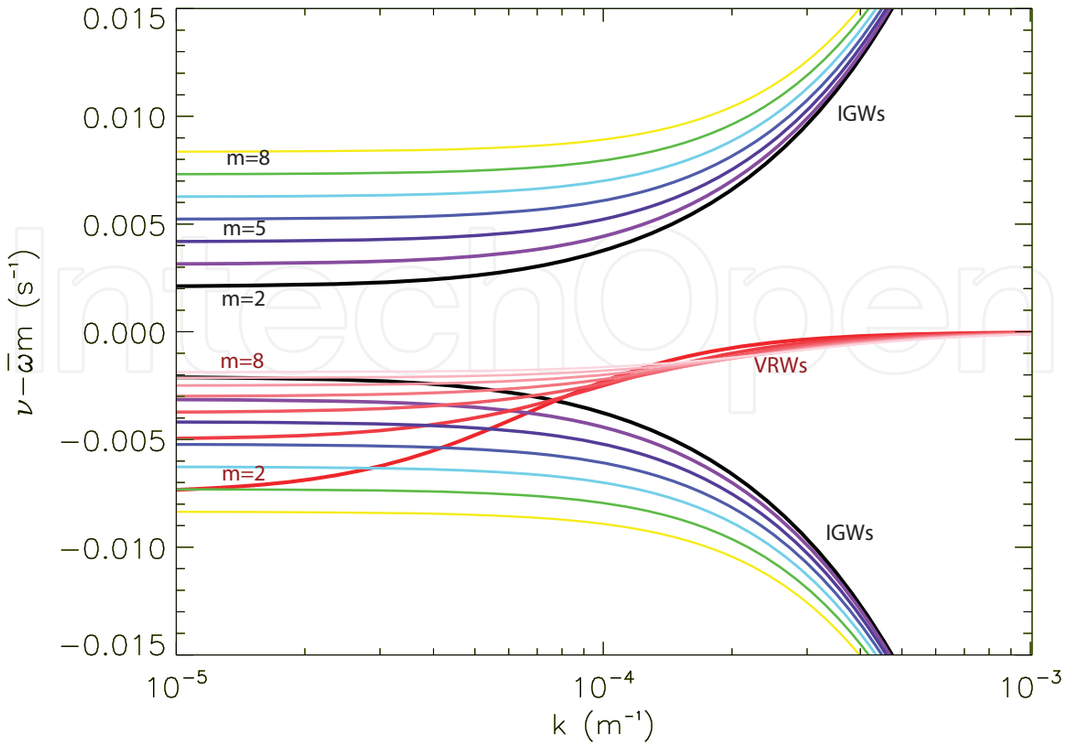


Fig. 1. Plot of the Doppler-shifted frequency $\nu - \bar{\omega}m$ versus radial wavenumber k for the inward and outwardly propagating inertia-gravity waves (IGWs) and vortex Rossby waves (VRWs) for azimuthal wavenumbers $m = 2 \ldots 8$. IGWs are plotted for a basic state vortex with $f = 5 \times 10^{-5}$ s^{-1}, $\bar{\omega} = 1 \times 10^{-4}$ s^{-1}, $\bar{h} = 100$ m, and at $r = 30$ km. The VRWs are plotted for a basic state vortex with $d\bar{\zeta}/dr = -5 \times 10^{-7}$ s^{-1} m^{-1}, $\bar{\omega} = 1 \times 10^{-4}$ s^{-1}, and at $r = 30$ km.

Multiplying $(hu)\cdot(23)$ and $(hv)\cdot(24)$, adding them together, and combining with the mass conservation equation (5), we obtain

$$\frac{\partial(K+gh)}{\partial t} + \frac{\partial[rhu(K+gh)]}{r\partial r} + \frac{\partial[hv(K+gh)]}{r\partial\phi} = 0, \tag{25}$$

where $K = (u^2 + v^2)/2$ is the kinetic energy and gh is the gravitational potential energy. By integrating (25) over the entire polar domain, we obtain

$$\frac{d}{dt}\iint (K+gh) r dr\, d\phi = 0, \tag{26}$$

which indicates that the total integrated energy is conserved in time. In an integrated sense, changes in gravitational potential energy must be balanced by equal changes in kinetic energy. By multiplying $r\cdot(2)$ and rewriting using the absolute angular momentum $M = rv + fr^2/2$ (or the angular momentum of an air parcel due to both the vortex and Earth's rotation) we obtain the absolute angular momentum principle

$$\frac{DM}{Dt} = -g\frac{\partial h}{\partial \phi}. \tag{27}$$

Equation (27) indicates that absolute angular momentum is materially conserved in the absence of the azimuthal torque $-g\partial h/\partial\phi$. This principle has profound implications for hurricane dynamics. In hurricanes, the radial pressure gradient force $g\partial h/\partial r$ is much larger than the azimuthal pressure gradient force $(g/r)\partial h/\partial\phi$, often M is nearly materially conserved above the boundary layer in real hurricanes. In the boundary layer, there exists friction so that as air parcels spiral inward they lose angular momentum. The near material conservation of M indicates that any mechanism that is able to move air radially inward to smaller radii will also cause the tangential winds to increase, and similarly air that moves radially outward will cause the tangential winds to decrease. This is analogous to the figure skater who spins faster when his or her arms are brought inward and vice versa. Additionally, asymmetric convection can create azimuthal torques to change M. Therefore an air parcel that spirals inward with a favorable azimuthal torque from asymmetric convection can rapidly increase its absolute angular momentum.

2.5 Eddy-mean flow interaction

In the preceding section, perturbations were assumed to be small in comparison to their means, which allowed us to neglect higher order terms. However, in many cases, the PV asymmetries are of sufficiently large magnitude so that a linear model is no longer valid. In this sense, the term “wave" should be replaced with the more general term “eddy", and the eddies may interact in nonlinear ways with the mean vortex. For example, in certain locations the eddies may spin-down the mean vortex while in other locations they may spin-up the mean vortex.

The eddy-mean flow interaction can be elegantly described using the isentropic formulation of Andrews (1983) and Andrews et al. (1987) reduced to our one-layer shallow water fluid. For the radial wind u, the mass-weighted azimuthal average is defined by $\hat{u} = \overline{hu}/\bar{h}$. The deviation from the ordinary average is defined by $v' = v - \bar{v}$, and the deviation from the mass-weighted average is defined by $u^* = u - \hat{u}$. Similar definitions hold for the other variables.

Applying $\overline{(\ )}$ to each term in (5) and noting that $\overline{hu} = \bar{h}\hat{u}$, we can write the azimuthal mean mass continuity equation as

$$\frac{\partial \bar{h}}{\partial t} + \frac{\partial (r\bar{h}\hat{u})}{r\partial r} = 0. \tag{28}$$

Similarly, applying $\overline{(\ )}$ to each term in (24) and noting that $\overline{hPu} = \bar{h}\hat{P}\hat{u} + \overline{hP^*u^*}$ we can write the azimuthal mean v equation as

$$\frac{\partial \bar{v}}{\partial t} + (f + \bar{\zeta})\hat{u} = -\overline{hP^*u^*}. \tag{29}$$

Now consider the radial momentum equation. Since both (28) and (29) contain $\hat{u}$, we would like to transform (23) into a prediction equation for $\hat{u}$. This requires putting (23) into a flux form before taking the azimuthal average. Thus, combining (23) and (5), we obtain the flux form

$$\frac{\partial (hu)}{\partial t} + \frac{\partial (rhuu)}{r\partial r} + \frac{\partial (hvu)}{r\partial \phi} - \left(f + \frac{v}{r}\right) hv + gh\frac{\partial h}{\partial r} = 0. \tag{30}$$

Taking the azimuthal average of (30), we obtain

$$\frac{\partial (\overline{hu})}{\partial t} + \frac{\partial (r\overline{huu})}{r\partial r} - \overline{\left(f + \frac{v}{r}\right) hv} + gh\overline{\frac{\partial h}{\partial r}} = 0. \tag{31}$$

Noting that $\overline{hu} = \bar{h}\hat{u}$, $\overline{huu} = \bar{h}\hat{u}\hat{u} + \overline{hu^*u^*}$, $\overline{h(\partial h/\partial r)} = \bar{h}(\partial\bar{h}/\partial r) + \overline{h'(\partial h'/\partial r)}$, and using the azimuthal mean continuity equation (28), we obtain the advective form (32).
Collecting the above results, we obtain the complete set of azimuthal mean equations

$$\frac{\mathcal{D}\hat{u}}{\mathcal{D}t} - \left(f + \frac{\bar{v}}{r}\right)\bar{v} + g\frac{\partial\bar{h}}{\partial r} = \mathcal{F}, \tag{32}$$

$$\frac{\mathcal{D}\bar{M}}{\mathcal{D}t} = r\mathcal{G}, \tag{33}$$

$$\frac{\mathcal{D}\bar{h}}{\mathcal{D}t} + \bar{h}\frac{\partial(r\hat{u})}{r\partial r} = 0, \tag{34}$$

where

$$\frac{\mathcal{D}}{\mathcal{D}t} = \frac{\partial}{\partial t} + \hat{u}\frac{\partial}{\partial r} \tag{35}$$

is the azimuthal mean material derivative, $\bar{M} = r\bar{v} + \frac{1}{2}fr^2$ is the azimuthal mean absolute angular momentum, and where

$$\mathcal{F} = -\frac{1}{\bar{h}}\left[\frac{\partial(r\overline{hu^*u^*})}{r\partial r} - \left(f + \frac{\bar{v}}{r}\right)\overline{h'v'} - \overline{\frac{(hv)'v'}{r}} + g\overline{h'\frac{\partial h'}{\partial r}}\right] \tag{36}$$

and

$$\mathcal{G} = -\overline{hP^*u^*} \tag{37}$$

are the eddy-induced effective mean radial and azimuthal forces per unit mass. By examining these equations, it is directly clear how the eddies interact with the mean flow. The mean radial momentum can be modified by the eddy-induced force $\mathcal{F}$ and the mean angular momentum can be changed by the eddy-induced torque $r\mathcal{G}$.

2.6 Numerical simulations

Numerical simulations presented in sections 3.1 and 3.2 were obtained using an f-plane pseudospectral shallow water model, with the Cartesian formulation of equations (3)-(5). The numerical solution was obtained on a 600 km $\times$ 600 km doubly periodic domain using 512 $\times$ 512 equally spaced points. After dealiasing of the quadratic advection terms in (3)-(5), the number of retained Fourier modes was 170 $\times$ 170, yielding an effective resolution of 3.52 km. A third order Adams-Bashforth time scheme was used with a time step of 5 s. Numerical diffusion terms were added to the right hand side of the Cartesian forms of (3)-(5), with a coefficient $\nu = 100$ m^2 s^{-1}. The Coriolis parameter $f = 1 \times 10^{-4}$ s^{-1} and the mean fluid depth $\bar{h} = 4077$ m. Numerical simulations presented in section 3.3 were performed using the nondivergent limit of the Cartesian formulations of (3)-(5), i.e. (3) combined with $\nabla^2\psi = \zeta$.

3. Internal dynamical processes

In this section the dynamical model and associated principles are used in conjunction with observations to illustrate barotropic aspects of the important internal dynamical processes responsible for hurricane structure and intensity variability: spiral rainbands, instabilities and mixing between the eye and eyewall, and concentric eyewall cycles.

3.1 Spiral bands

One of the most distiguishable features on tropical cyclones are spiral rain bands. If spiral rainbands are thought of as small amplitude propagating perturbations on a basic state vortex, we might expect that linear wave theory may be able to explain some aspects of their structure and propagation speeds. An earlier view (Kurihara, 1979; Willoughby, 1978) was that spiral bands were inertia-gravity waves. In order to illustrate how spiral bands may be viewed as propagating inertia-gravity waves, we assume $d\bar{\zeta}/dr = d\bar{h}/dr = 0$ and a constant angular velocity $\bar{\omega}$ in (13)-(15) to obtain

$$\left(\frac{\partial}{\partial t} + \bar{\omega}\frac{\partial}{\partial \phi}\right)\nabla^2\psi' + \bar{\eta}\nabla^2\chi' = 0 \tag{38}$$

$$\left(\frac{\partial}{\partial t} + \bar{\omega}\frac{\partial}{\partial \phi}\right)\nabla^2\chi' - \bar{\eta}\nabla^2\psi' + g\nabla^2 h' = 0 \tag{39}$$

$$\left(\frac{\partial}{\partial t} + \bar{\omega}\frac{\partial}{\partial \phi}\right)h' + \bar{h}\nabla^2\chi' = 0, \tag{40}$$

Assuming separable solutions of the form $h'(r,\phi,t) = \hat{h}(kr)\exp[i(m\phi - \nu t)]$ (and similar definitions hold for the other variables), a ordinary differential Bessel equation is obtained which governs the radial structure of the waves. The outward propagating solution to this equation are Hankel functions $H_m^{(1)}(kr)$, which are given in terms of the Bessel function $J_m(kr)$ and the Neumann function $Y_m(kr)$ by $H_m^{(1)}(kr) = J_m(kr) + iY_m(kr)$ as

$$\begin{pmatrix}\chi'(r,\phi,t)\\ \psi'(r,\phi,t)\\ h'(r,\phi,t)\end{pmatrix} = -\frac{h_0}{\bar{h}k^2}\begin{pmatrix}i(\nu-\bar{\omega}m)\\ f+2\bar{\omega}\\ -\bar{h}k^2/h_0\end{pmatrix}H_m^{(1)}(kr)e^{i(m\phi-\nu t)}, \tag{41}$$

where h_0 is an arbitrary constant, and where the radial wavenumber k and the frequency ν are related by (16). The relative vorticity and divergence associated with the streamfunction and velocity potential according to (7) are

$$\begin{pmatrix}\delta'(r,\phi,t)\\ \zeta'(r,\phi,t)\end{pmatrix} = h_0\begin{pmatrix}i(\nu-\bar{\omega}m)/\bar{h}\\ (f+2\bar{\omega})/\bar{h}\end{pmatrix}H_m^{(1)}(kr)e^{i(m\phi-\nu t)}, \tag{42}$$

From (6) we find that the perturbation radial velocity $u' = (\partial\chi'/\partial r) - (\partial\psi'/r\partial\phi)$ and the perturbation azimuthal velocity $v' = (\partial\chi'/r\partial\phi) + (\partial\psi'/\partial r)$ can be written as

$$\begin{pmatrix}u'(r,\varphi,t)\\ iv'(r,\varphi,t)\end{pmatrix} = \frac{ih_0}{\bar{h}k^2}\cdot\begin{pmatrix}(\nu-\bar{\omega}m+f+2\bar{\omega})(m/r)H_m^{(1)}(kr)\\ -(\nu-\bar{\omega}m)kH_{m-1}^{(1)}(kr)\\ (\nu-\bar{\omega}m+f+2\bar{\omega})(m/r)H_m^{(1)}(kr)\\ -(f+2\bar{\omega})kH_{m-1}^{(1)}(kr)\end{pmatrix}e^{i(m\varphi-\nu t)}, \tag{43}$$

where we have made use of the Hankel function derivative relation $dH_m^{(1)}(kr)/dr = kH_{m-1}^{(1)}(kr) - (m/r)H_m^{(1)}(kr)$. Equations (41)–(43) consititute the exact analytic solution to (38)-(40) for outwardly propagating cylindrical waves.

In Figure 2a, a large spiral rainband observed in Hurricane Alex on 1925 UTC is shown, and in Figure 2b the linear solution of $h'(r,\phi)$ is shown with overlayed vectors of $u'(r,\phi)$ and

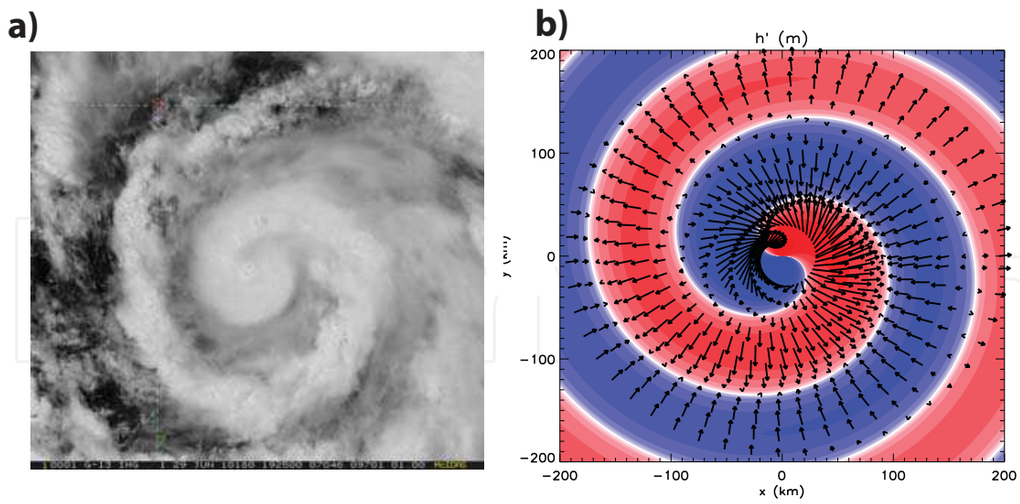


Fig. 2. Panels: a) Observed large spiral rainband in Hurricane Alex on 1925 UTC on June 29, 2010 (left panel), and b) Linear solution for h' with overlayed vectors of u' and v' for the shallow water equations in polar space. The constants used are $\bar{h} = 4288$ m, $\bar{\omega} = 5 \times 10^{-4}$ s^{-1}, $k = 4 \times 10^{-5}$ m^{-1}, $f = 3.7 \times 10^{-5}$ s^{-1}, $h_0 = 10$ m, and $m = 1$. Vectors are plotted in the region 30 km $< r <$ 200 km. Panel a) is courtesy of NOAA/NESDIS/RAMMB in Fort Collins, CO, USA.

$v'(r, \phi)$. Here, the red region denotes positive h' (fluid depth slightly higher) and the blue region denotes negative h' (fluid depth slightly lower). In this particular instant the large spiral rainband of Alex resembles the linear solution to the shallow water equations with azimuthal wavenumber $m = 1$. Note that the perturbation winds are highly divergent and that the orientation and the divergence pattern of the winds with respect to the perturbation height field favors outward propagation of the wave. An propagating spiral region of low level convergence could create shallow or deep convective activity similar to the observations of Alex. However, in order to be sure the frequencies are that of the observed wave, the linear theory would need to be compared.

Another viewpoint is that spiral bands are vortex Rossby waves (MacDonald, 1968; Guinn & Schubert, 1993; Montgomery & Kallenbach, 1997; Chen and Yau, 2001). Their arguments were based off the fact that spiral bands are often observed to propagate azimuthally slower than the mean flow, and the fact that the bands became tighter moving radially outward, similar to PV filaments. Since vortex Rossby waves are confined to live where there exists a radial PV gradient, radial propagation can no longer continue once the waves propagate outward to a certain stagnation radius. At this time, and at earlier times, the symmetrizing effect of the swirling winds tends to shear the waves into tightly wrapped spirals. Eventually the waves decay and axisymmetrization is complete.

Using the numerical model described in section 2.5, a simulation was run with an initially elliptical PV field. Hurricanes are sometimes observed to have distinct elliptical shapes in the inner-core (Kuo et al., 1999; Reasor et al., 2000). In polar coordinates, the initial vorticity field was specified by

$$\zeta(r, \phi, 0) = \zeta_0 \begin{cases} 1 & 0 \leq r \leq r_i \alpha(\phi) \\ 1 - f_\lambda(r') & r_i \alpha(\phi) \leq r \leq r_o \alpha(\phi), \\ 0 & r_o \alpha(\phi) \leq r \end{cases} \tag{44}$$

where $\alpha(\phi) = [(1-\epsilon^2)/(1-\epsilon^2\cos^2(\phi))]^{1/2}$ is an ellipticity augmentation factor for the ellipse $(x/a)^2 + (y/b)^2 = 1$ (where a is the semi-major axis and b is the semi-minor axis) with eccentricity $\epsilon = (1-(b^2/a^2))^{1/2}$. Here, ζ_0 is the maximum vorticity at the center, $f_\lambda(r') = \exp[-(\lambda/r')\exp(1/(r'-1))]$ is a monotonic shape function with transition steepness parameter λ, $r' = (r - r_i\alpha(\phi))/(r_o\alpha(\phi) - r_i\alpha(\phi))$ is a nondimensional radius, and r_i and r_o are the radii where the vorticity begins to decrease and where it vanishes, respectively. For the special case of $\alpha(\phi) = 1$ the field is axisymmetric. For the experiment conducted, $\zeta_0 = 3.0 \times 10^{-3}$ s^{-1}, $\lambda = 2.0$, $\epsilon = 0.60$, and r_i and r_o were set to 10 km and 110 km, respectively. The balanced mass field was determined by solving the nonlinear balance equation, and the initial divergence was set to zero everwhere in the domain.

In Figure 3a, spiral rainbands observed in radar imagery are shown as Hurricane Hugo (1989) made landfall in Charleston, South Carolina. In Figure 3b, spiral rainbands are shown in Hurricane Danielle (2010) in the visible satellite imagery. Note that in both of these panels, the spiral bands are tightly wrapped, or have a larger radial wavenumber. Figure 3c depicts the evolution of $P = (\bar{h}/h)(f+\zeta)$ in the numerical simulation, with brighter colors denoting larger PV. The first panel is the initial condition and each subsequent panel is 1.25 h apart. As the ellipse symmetrizes, two PV filaments are visible. These PV filaments are vortex Rossby waves which are breaking anticyclonically due the swirling winds of the vortex outside the radius of maximum wind, and resemble the tighter spiral bands observed in real hurricanes. Eventually the elliptical PV field symmetrizes into a axisymmetric monopole. In the real atmosphere, external factors such as vertical and horizontal shear as well as internal processes such as convective activity can excite vortex Rossby waves. For monotonic vortices, these waves will generally decay with time, creating spiral PV filaments resembling spiral bands. As stated earlier, while inner spiral rainbands are likely sheared vortex Rossby waves, the outer bands may often be outwardly radiating inertia-gravity waves. Guinn and Schubert (1993) also hypothesized that the outer bands may form during a combined barotropic-baroclinic instability of the intertropical convergence zone. In this sense, the large PV filaments formed from this breakdown are breaking Rossby-like waves, but not vortex Rossby waves.

There is continuing debate on the net effects of spiral rainbands on TC intensity. In a forced context, where the effect of deep convection are parameterized by region of enhanced PV, vortex Rossby wave theory indicates that axisymmetrization of PV anomalies (Carr & Williams, 1989) will spin-up the mean winds as the waves propagate radially outward (Montgomery & Kallenbach, 1997). In an unforced context (as described here), the anticyclonic wave-breaking outside the vortex core actually spins down the vortex winds there. The real atmosphere is much more complicated. Since spiral bands have diabatic heating, there can be associated downdrafts and subsidence in between successive bands. The spiral bands can also cut off inflow into the core of the vortex, resulting in potential weakening (Barnes et al., 1983). Further research is certainly warranted on the net effects of spiral bands, either generated by vortex Rossby or inertia-gravity waves on hurricane intensity.

3.2 Eyewall processes

The eyewall of intense or intensifying hurricanes is often observed to be a annular tower of elevated potential vorticity (Kossin & Eastin, 2001; Möller & Smith, 1994), that extends from the surface to approximately 8-12 km in height. Thus at any vertical level the radial gradient of azimuthal mean PV changes sign moving from the vortex center to the boundaries. This satisfies the Charney-Stern necessary condition for dynamic instability. In the three-dimensional atmosphere, this instability due in part to both barotropic and

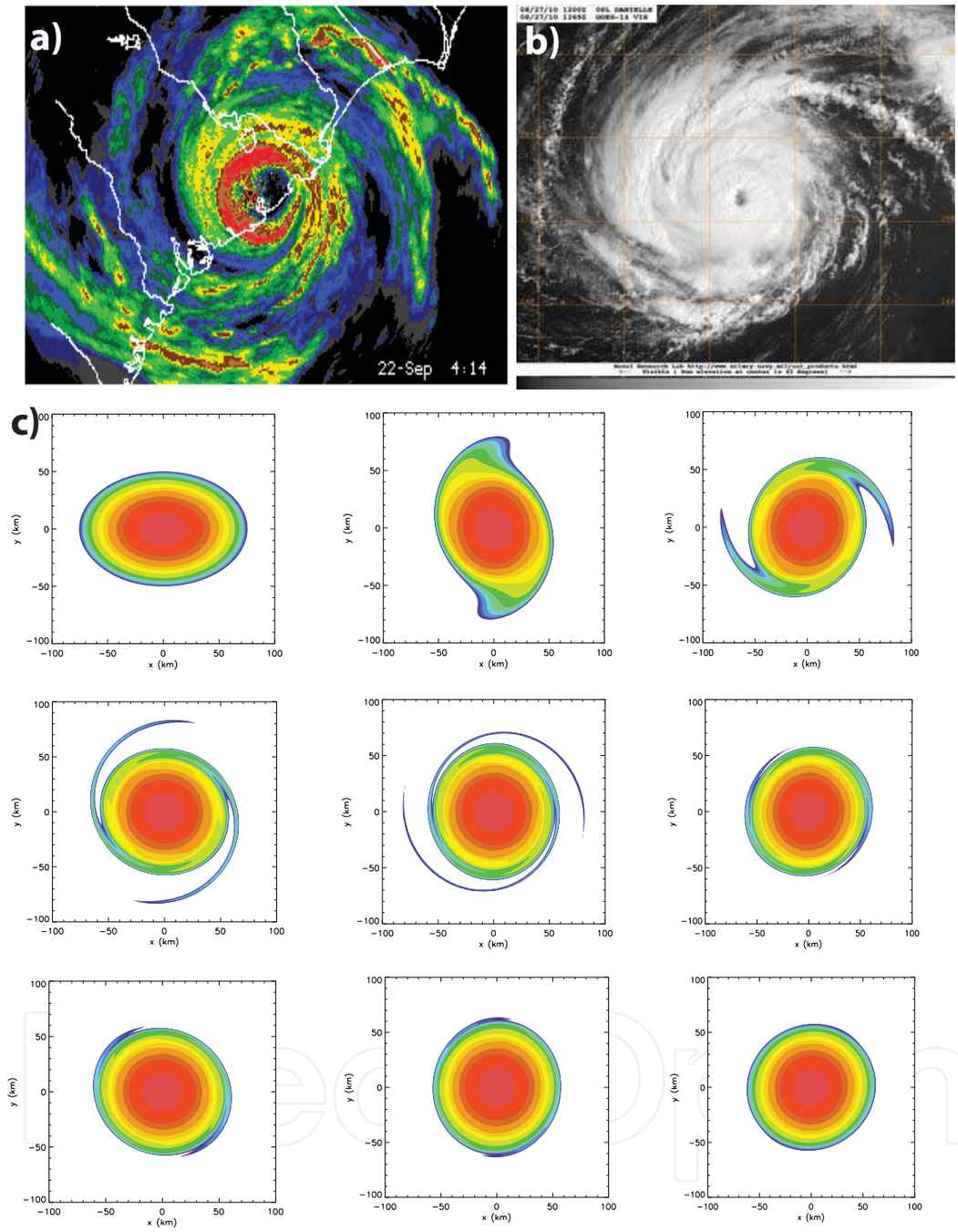


Fig. 3. Panels: a) Spiral rainbands observed in Hurricane Hugo as it made landfall on September 22, 1989 at 0414 UTC, b) Spiral rainbands observed in visible satellite imagery of Hurricane Danielle on August 23, 2010. c) Evolution of the elliptical PV field in a shallow water model. The first figure is the initial condition and each subsequent figure is 1.25 h apart. Panels (a) and (b) are courtesy of NOAA/AOML/Hurricane Research Division in Miami, FL, USA.

baroclinic instabilities, with the former instability being attributed to the large radial shear of the tangential wind as well as the curvature vorticity, and the latter instability being owed to the vertical shear of the vortex tangential wind. We will focus here on barotropic instability and ensuing mixing process between the eyewall and eye.

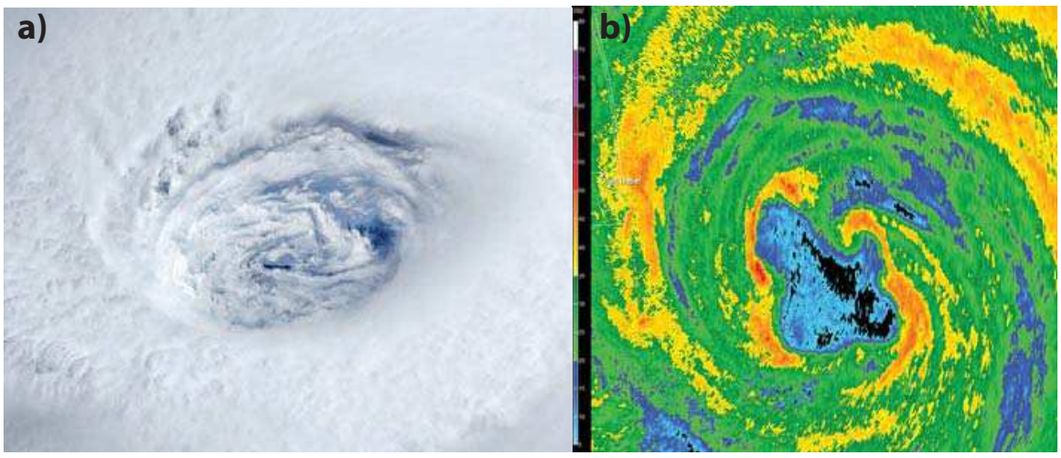


Fig. 4. Panels: a) Vortical swirls in the eye of Hurricane Igor (2010) observed from MODIS, and b) A wavenumber-4 pattern in the radar reflectivity in Hurricane Dolly as it approached the Texas coast at 1052 UTC on July 23, 2008. Panel a) is courtesy of NASA and panel b) is courtesy of the National Weather Service in Brownsville, TX, USA.

In Figure 4, two images are shown to illustrate some observed inner-core asymmetries and eye-eyewall mixing in hurricanes. In Figure 4a, vortical swirls observed at low levels in the eye of Hurricane Igor are shown and in Figure 4b, a wavenumber-4 pattern is shown in Hurricane Dolly (2008) as it approached southern Texas. Polygonal eyewall shapes, and eye mesovortices have been hypothesized by Schubert et al. (1999) to all be part of an intrinsic mixing process occuring between the eye and eyewall of hurricanes resulting from dynamic instability of the eyewall PV hollow tower.

Barotropic instability on a circular vortex is best understood by considering the interaction of two counter-propagating vortex Rossby waves. Consider a ring of elevated vorticity as shown in Figure 5. As shown in section 2, the local azimuthal phase velocity for disturbance vorticity $\zeta'(r,\phi)$ is

$$c_\phi = \bar{v}(r) + \frac{d\bar{\zeta}/dr}{k^2 + m^2/r^2}. \tag{45}$$

The corresponding local wave angular phase velocity is

$$\omega_\phi = \bar{\omega}(r) + \frac{1}{r}\frac{d\bar{\zeta}/dr}{k^2 + m^2/r^2}, \tag{46}$$

Now consider two Rossby waves which exist on the inner and outer edge of the vorticity annulus in Figure 5. For the inner wave, $d\bar{\zeta}/dr$ is positive, while for the outer wave, $d\bar{\zeta}/dr$ is negative. According to (46), the inner wave has a larger angular velocity than the vortex angular velocity, while the outer wave has a smaller angular velocity than the vortex angular velocity. Thus, the inner wave prograde relative to its local flow, and the outer wave retrogrades relative to its local flow. Since the angular velocity profile for this ring has a minimum at the location of the first basic state vorticity gradient, and a

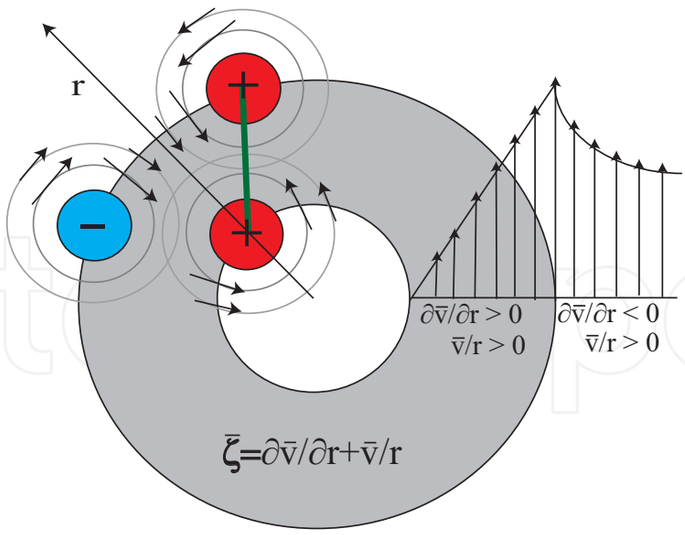


Fig. 5. Conceptual model of the interaction of counter-propagating vortex Rossby waves on a ring of elevated vorticity. Positive sign indicates a cyclonic vorticity anomaly, and negative sign indicates a anti-cyclonic vorticity anomaly. At this time the inner and outer vorticity anomalies are locked in phase (thick green line) with upshear tilt, and the circulation associated with each anomaly is advecting the other anomaly, leading to distortion of the initially axisymmetric ring.

maximum at the location of the second basic state vorticity gradient, it is possible for the two waves to be phase-locked, or have the same absolute absolute angular velocity. If the waves become phase-locked with the disturbance vorticity tilted upshear, as shown in Figure 5, each anomaly is in the optimum phase to interact with the other, eventually leading to distortion of the axisymmetric ring. Note in particular that the cyclonic circulation associated with the outer vorticity anomaly is advecting the inner anomaly inward (enhanced by the anticyclonic anomaly next to it), while the circulation of the inner vorticity anomaly is advecting the outer anomaly radially outward. Clearly, the interaction of vorticity anomalies is ehanced for thinner rings and with rings of larger basic state vorticity. A mathematically rigorous description of the interaction of these counter-propagating vortex Rossby waves in the inner-core is provided by Schubert et al. (1999). Interestingly, this barotropic instability can also exist in the outer region of the tropical cyclone (Peng et al., 2008), affecting its outer structure and intensity.

In the early phase of barotropic instability, both the inner and outer vortex Rossby waves are growing exponentially with time. After a number of *e*-folding times, the infinitesimal perturbations have grown to significant amplitude such that the linearized equations are no longer valid. The flow now is governed by the nonlinear PV equation (8), where the advection terms are of principal importance. In order to understand the resultant vortex structure and intensity change resulting from barotropic instability, we must use a numerical model to simulate the PV advection. In the real atmosphere, there also exists diffusion, which can be thought of as a parameterized eddy viscosity coefficient assuming flux gradient theory. This new PV equation

$$\frac{\partial P}{\partial t} + u\frac{\partial (rP)}{r\partial r} + \frac{v}{r}\frac{\partial P}{\partial \phi} = \nu \nabla^2 P, \tag{47}$$

governs advective mixing (or the combined effects of advection and diffusion) in a barotropic framework, where ν is the eddy viscosity coefficient. Given a PV distribution at some initial time, equation (47) governs the evolution of PV at subsequent times. The advecting winds u and v change each time step, and are determined by the invertibility principle discussed previously. The winds also advect an arbitrary passive tracer $c(r, \phi, t)$, where

$$\frac{\partial c}{\partial t} + u\frac{\partial (rc)}{r\partial r} + \frac{v}{r}\frac{\partial c}{\partial \phi} = \nu \nabla^2 c. \tag{48}$$

In the real atmosphere, this quasi-passive tracer could be water vapor molecules or a derived thermal property such as equivalent potential temperature. It is insightful to examine the interplay of the advection and diffusion in (47) and (48). Advection, or more specifically differential advection (where the advecting winds vary in space and time), acts to create a complicated geometric structure of an arbitrary active or passive tracer. However, true mixing cannot occur unless air parcels exchange properties with one another through diffusion. Thus, advective mixing is due to the combined effects of reversible advection and irreversible diffusion. In the view of Nakamura (1996), differential advection acts to deform tracer contours so that there is more interface for diffusion to act. He provided a derivation of a modified “effective diffusion" equation, where the effects of the differential advection are parameterized by a larger diffusion coefficient. Hendricks & Schubert (2009) applied this effective diffusivity diagnostic to evolving barotropic hurricane-like vortices, and determined the location and magnitude of chaotic mixing and partial barrier regions. Mixing regions were located near breaking vortex Rossby waves, while partial barrier regions were located near tangential jets.

A numerical simulation was performed in the shallow water model for a PV ring similar to that shown in Figure 5. The initial ring was defined by

$$\bar{\zeta}(r,0) = \begin{cases} \zeta_1 & 0 \le r \le r_1 \\ \zeta_1 S(\frac{r-r_1}{r_2-r_1}) + \zeta_2 S(\frac{r_2-r}{r_2-r_1}) & r_1 \le r \le r_2 \\ \zeta_2 & r_2 \le r \le r_3, \\ \zeta_2 S(\frac{r-r_3}{r_4-r_3}) + \zeta_3 S(\frac{r_4-r}{r_4-r_3}) & r_3 \le r \le r_4 \\ \zeta_3 & r_4 \le r \le \infty \end{cases} \tag{49}$$

where $\zeta_1 = 0$, $\zeta_2 = 3 \times 10^{-3}$ s^{-1}, and ζ_3 is set to a minimal negative value so that the circulation vanishes at the boundary. The radii $r_1 = 20$ km, $r_2 = 24$ km, $r_3 = 38$ km, and $r_4 = 42$ km, and $S(s) = 1 - 3s^2 + 2s^3$ is a cubic Hermite shape function that provides smooth transition zones. The eye is defined as the region where $r < r_1$, the eyewall is defined as the region between r_2 and r_3, and the transition zones are defined as the regions between r_1 and r_2, and r_3 and r_4. To initiate the instability process, a broadband perturbation (impulse) was added to the basic state vorticity (6) of the form

$$\zeta'(r,\phi,0) = \zeta_{\text{amp}} \sum_{m=1}^{8} \cos(m\phi + \phi_m) \quad \times \begin{cases} 0 & 0 \le r \le r_1, \\ S(\frac{r_2-r}{r_2-r_1}) & r_1 \le r \le r_2, \\ 1 & r_2 \le r \le r_3, \\ S(\frac{r-r_3}{r_4-r_3}) & r_3 \le r \le r_4, \\ 0 & r_4 \le r < \infty, \end{cases} \tag{50}$$

where $\zeta_{\text{amp}} = 1.0 \times 10^{-5}$ s^{-1} is the amplitude and ϕ_m the phase of azimuthal wavenumber m. For this set of experiments, the phase angles ϕ_m were chosen to be random numbers in the range $0 \leq \phi_m \leq 2\pi$. In real hurricanes, the impulse is expected to develop from a wide spectrum of background convective motions. As in the ellipse, the height $h(r, \phi)$ was determined by solving the nonlinear balance equation using the basic state vorticity and the initial divergence $\delta(r, \phi)$ was set to zero.

In Figure 6, the nonlinear evolution of the PV ring above in the shallow water model is shown. In Figure 6a, the asymmetric PV and asymmetric velocity vectors are shown at $t = 2$ h in this simulation, and in Figure 6b the same asymmetric velocity vectors are overlayed on the perturbation height field. Examining Figure 6a, note that there are two vortex Rossby wave-trains that exist at locations of the the inner and outer PV gradients, respectively. Both wave-trains are phase-locked and propagating at the same angular velocity relative to Earth. Note that the most unstable mode for this PV ring is $m = 3$, and that outer PV anomalies are tilted upshear with respect to the inner PV anomalies. Also note that the perturbation winds are anticyclonic for negative PV anomalies (blue) and cyclonic for positive PV anomalies (red), and that upshear phase-locking is allowing the inner and outer PV anomalies to optimally interact with one another, leading to distortion of the initial axisymmetric ring, similar to the conceptual model in Figure 5. In Figure 6b, note that cyclonic anomalies are associated with lower heights, and anticyclonic anomalies are associated with higher heights. Finally, note that the winds are approximately parallel to the contours of constant perturbation height, which indicates that these vortex Rossby waves are largely balanced. If the center of the vortex is viewed as the North Pole, these vortex Rossby waves are quite similar to large-scale planetary Rossby waves responsible for low frequency variability in weather patterns. The vortex Rossby wave patterns in this barotropic model are similar to full-physics model simulations by Wang (2002a). In their simulation, cyclonic PV perturbations on the vortex are coupled with updrafts and low level convergence, and as such in reality, *convectively coupled* vortex Rossby waves often exist in hurricanes. This coupled wave has been hypothesized by Montgomery & Enagonio (1998) and Möller & Montgomery (2000) to be important for tropical cyclogenesis as well as hurricane intensity change.

In Figure 6c, the evolution of the PV ring is shown for the entire experiment, with each panel being 5 h apart. As the inner and outer vortex Rossby waves grow in tandem, the circular ring is distorted into a polygonal shape with straight line segments. The inner vortex Rossby wave breaks cyclonically drawing low PV air from the eye into the eyewall. Similarly the outer vortex Rossby wave breaks anticyclonically similar to the ellipse, drawing high PV from the eyewall outward in the form of PV filaments. During the evolution of this ring, the eye contracts in an asymmetric fashion, and the vortex slowly symmetrizes into a monopole. Interestingly, Hodyss & Nolan (2008) found that these polygonal shapes can also form when the Rossby-inertia gravity wave instability is the most unstable mode.

During these PV mixing events, significant changes can occur in the vortex structure and intensity. Equation (33) can be rewritten as

$$\frac{\partial \bar{M}}{\partial t} = -(f + \bar{\zeta}) r \hat{u} - r\overline{hP^* u^*} \tag{51}$$

where the left hand side is the local change in azimuthal mean angular momentum, the first term on the right hand side is the change in $\bar{M}$ due to the mean torque, and the second term on the right hand side is the change in $\bar{M}$ due to the eddy torque.

In Figure 7, the angular momentum budget for this simulation was computed from 0–35 h. The initial radius of maximum wind is at the edge of the PV ring, or approximately at $r = 42$

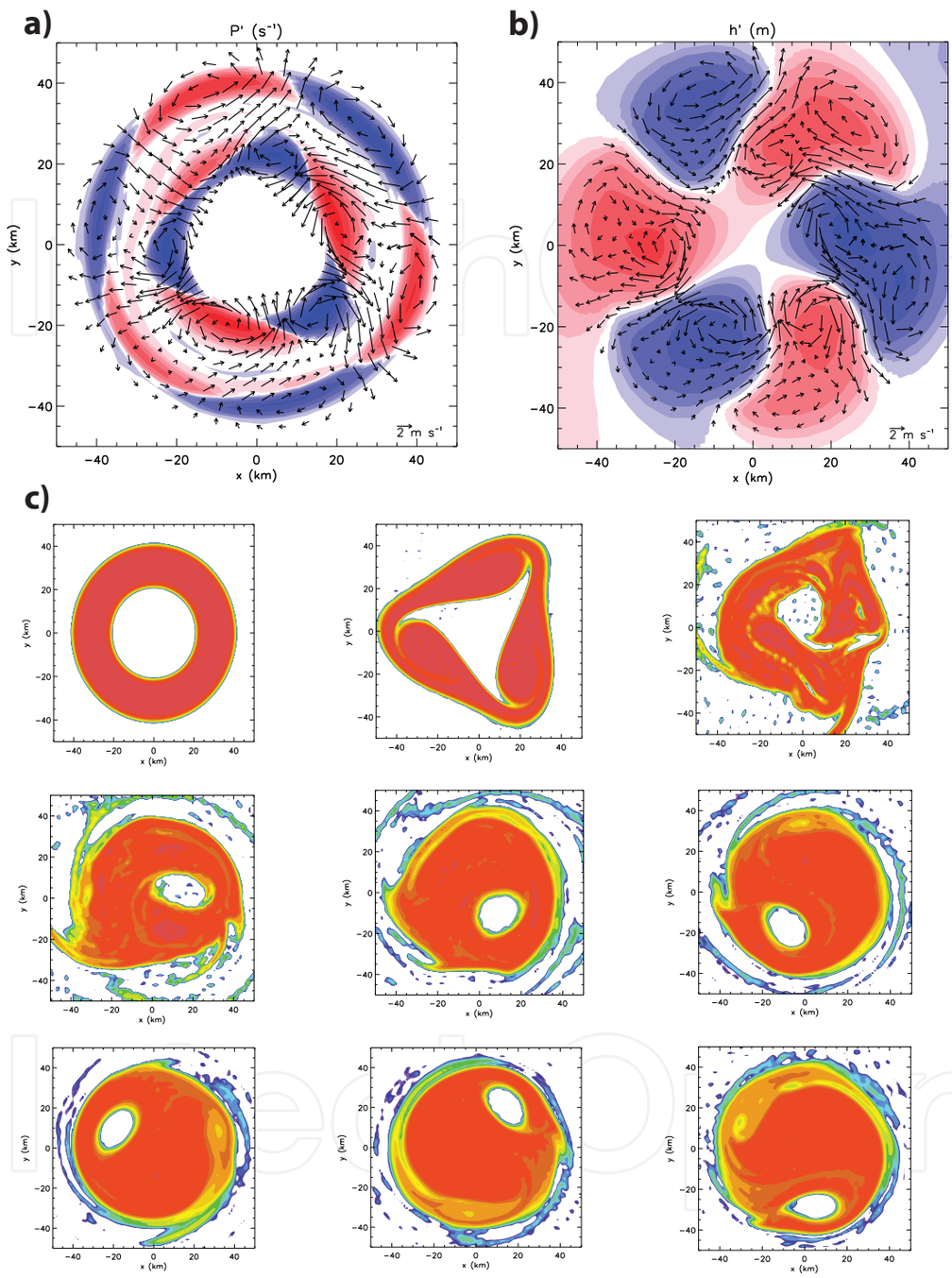


Fig. 6. Panels: a) Asymmetric PV with asymmetric wind vectors showing the most unstable mode of $m = 3$. b) Asymmetric wind vectors overlayed on the perturbation height field. c) The evolution of PV for the ring experiment in the shallow water model. The first figure is the initial condition and each subsequent figure is 5 h apart. In panels a) and b), vectors are plotted in the region 15 km $< r <$ 45 km, and red (blue) shading denotes positive (negative) values.

km. Three curves are plotted. The “ACTUAL" curve depicts the $\Delta\bar{M}$ due to the left hand side of (7), and the “MEAN" and “EDDY" curves depict the integration of the left hand side terms from 0–35 h using the trapezoidal rule on the 15-minute resolution output. Since PV mixing is a highly asymmetric process, the mean term is approximately zero everywhere. This is largely because $\hat{u}$ is nearly zero. However, in real hurricanes with inflow at lower levels, this term would contribute positively to the change in $\bar{M}$ at lower levels. The dominant term is the eddy-induced term. The eddies exert a positive torque in the region $0 < r < 35$ km and a negative torque in the region $35 < r < 70$ km. Viewing this in terms of the mean tangential momentum $\bar{v}$, this corresponds to a $\Delta\ \bar{v} = 25$ m s^{-1} at $r = 20$ km and $\Delta\ \bar{v} = -5$ m s^{-1} at $r = 40$ km. Additionally the radius of maximum wind contracts inward, and the larger winds at smaller radii increase the v^2/r term in the gradient wind balance equation 11, causing the height (or pressure) field to be lower after PV mixing than the initial condition. This is the dual nature of PV mixing with regard to hurricane intensity in a barotropic framework: it simultaneously lowers the central pressure and maximum wind (Kossin & Schubert, 2001; Rozoff et al., 2009; Hendricks et al., 2009). Results from simulation of three-dimensional unstable baroclinic vortices in a primitive equation model support these barotropic results (Hendricks & Schubert, 2010). However since observations and full-physics hurricane simulations rarely show that hurricanes simultaneously lower their central pressure and maximum wind (Wang, 2002b), it is possible that moist processes and boundary layer processes modify these results to some degree in the real atmosphere.

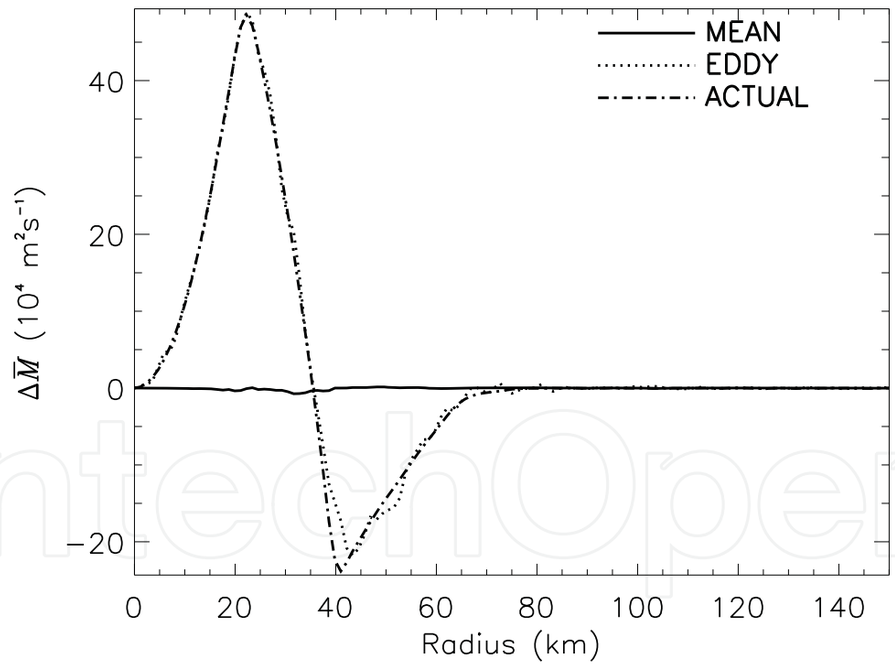


Fig. 7. Absolute angular momentum budget for the ring PV field simulation from 0-35 h.

Another interesting aspect of PV mixing is the horizontal mixing of quasi-passive tracers. Since many intense hurricanes have low level cloud swirls (i.e., airborne condensate) in the eye, it is likely that there is an internal mixing process occuring quite regularly, affecting structure and intensity. At low levels in the eye of hurricanes, there exists a very warm moist air mass (Eastin et al., 2002). In fact, the highest equivalent potential air in the hurricane is typically at low levels in the eye. During the breakdown of the PV ring, the inner breaking

vortex Rossby wave can mix this high energy air back into the eyewall, giving the air extra buoyancy as it rises in the deep cumulonimbus convection of the eyewall. This intensification mechanism has been studied in recent work (Cram et al., 2007; Montgomery et al., 2006; Persing & Montgomery, 2003), and also has implications for the maximum intensity that a hurricane may achieve in a given environment.

3.3 Concentric eyewall cycles

Another internal process that can cause significant structural and intensity variability are concentric eyewall (or eyewall replacement) cycles, which encompass the formation of the secondary eyewall, and its eventual contraction and replacement of the inner eyewall. Aircraft observations of Hurricane Gilbert (1988) (Black & Willoughby, 1992) indicated the presence of concentric eyewalls structure in their radar reflectivity. Approximately 12 hours after reaching its minimum sea level pressure of 888 hPa, Hurricane Gilbert displayed concentric eyewalls and quickly followed by the eyewall replacement cycle where the inner eyewall dissipated and storm weakened. The radar observation of typhoon Lekima (2001) near Taiwan (Kuo et al., 2004) indicates a huge area of convection outside the core vortex wraps around the inner eyewall to form concentric eyewalls in about 12 hours. Kuo et al. (2008) also reported cases of passive microwave data that the formation of a concentric eyewall from organization of asymmetric convection outside the primary eyewall into a symmetric band that encircled the eyewalls. Two such concentric eyewalls examples are shown in Fig. 8 for typhoons with for Typhoons Dujuan (2003) and Imbudo (2003). The time interval is approximately 12 h, and estimated maximum winds are indicated at the top of the image.

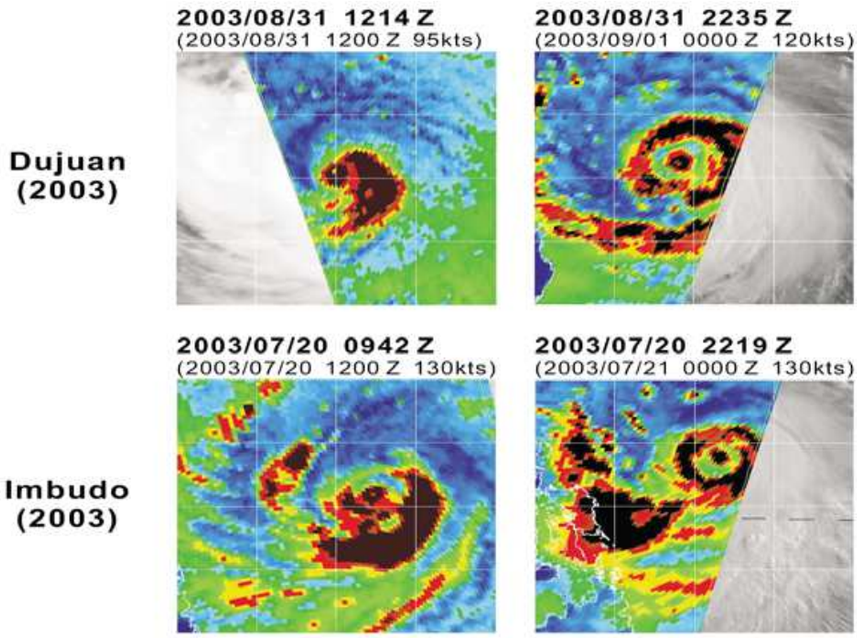


Fig. 8. Passive microwave image sequence for two western Pacific typhoons with concentric eyewalls (Dujuan and Imbudo). For each typhoon the time interval is approximately 12 h, and the estimated maximum winds are indicated at the top of the image (courtesy of Naval Research Laboratory, Monterey, CA, USA)

Dritschel & Waugh (1992) described the general interaction of two barotropic vortices with equal vorticity but with different sizes and separation distances. They performed experiments on the f-plane by varying two parameters, the ratio of the vortex radii and the separation distances normalized by the radius of the larger vortex. The resulting end states can be classified according to the two parameters into elastic interaction, merger, and straining out regimes. The elastic interaction involves distortion to the vortices in a mutual cyclonic rotation. The merger regime involved part of the smaller vortex being removed, and some of it being incorporated into the larger vortex. In the straining out regime, a thin region of filamented vorticity bands surrounding the central vortex with no incorporation into the central vortex. Many observed cases of tropical cyclone interactions resemble the idealized simulation of Dristchel and Waugh (Kuo et al., 2000; Lander & Holland, 1993; Larson, 1975; Prieto et al., 2003). Moreover, the straining out regime appeared to resemble the concentric eyewalls with a moat. However, the outer bands which result from the smaller vortex are much too thin to be identified with the outer eyewall of a tropical cyclone.

An important issue in the formation of concentric eyewalls appears to be the development of the symmetric structure from asymmetric convection. It appears that the formation of concentric eyewall has two important aspects: (i) an existing asymmetric potential vorticity distribution is organized by horizontal advective processes and (ii) the potential vorticity is diabatically enhanced during the organization process. Although both aspects are important, it is useful to isolate (i) through the study of highly idealized barotropic model. The dynamics can be idealized as the interaction of a small and strong vortex (representing the tropical cyclone core) with a large and weak vortex of various spatial scales (representing the vorticity induced by the moist convection outside the core vortex). This interaction of a strong and small vortex with a large and weak vortex was not studied by Dritschel & Waugh (1992) as their vortices are of the same strength, and their larger vortex was always the “victor" and the smaller vortex was the one being partially or totally destroyed. Kuo et al. (2004) introduced a new parameter “vorticity strength ratio" to the binary vortex interaction and adds a new dimension to the Dristchel-Waugh parameter space. As a result, binary interactions manifest a new stable end state: concentric vorticity structure. The axisymmetrization of positive vorticity perturbations around a strong and tight core of vorticity to produce concentric eyewall structure is studied in detail by Kuo et al. (2004; 2008).

To illustrate the barotropic dynamics of concetnric eyewalls formation, we first illustrate the straining out effect of the vortex. The straining out effect is due to the strong differential rotation outside the radius of maximum wind produces vorticity filaments. The strain effect may be quantified with the filamentation time τ_{fil}, in the nondivergent flow

$$\tau_{\text{fil}} = 2(S_1^2 + S_2^2 - \zeta^2)^{-\frac{1}{2}}, \tag{52}$$

provided $S_1^2 + S_2^2 > \zeta^2$, and where S_1 and S_2 are the stretching and shear deformation, respectively (Rozoff et al., 2006). The filamentation dynamics and its role to the moat formation was discussed by Rozoff et al. (2006). The filamentation time decreases as the strain flow strengthens. The presence of local vorticity field may offset the straining flow and lengthen the filamentation time. Figure 9 shows the vorticity fields at t = 0, 6, and 12 h for the straining out experiments. During the first 6 hours of the integration, the neighboring weak vortices become distorted into an approximately elliptical shape. As a result of the motion induced by its own vorticity, this ellipse turns counterclockwise, just as in the idealized Kirchhoff ellips solution (Kuo et al., 1999). Thus, one tip of the ellipse moves closer to the strong core vortex, while the other moves father away. The part of the weaker vorticity region

that is closest to the strong core vortex is then rapidly strained out and wound around the core vortex at close radius.

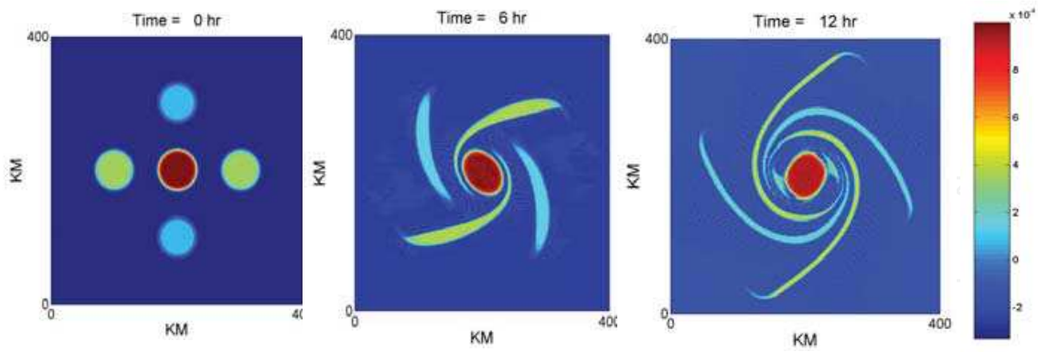


Fig. 9. Vorticity fields at t = 0, 6, 12 h in the straining out experiments.

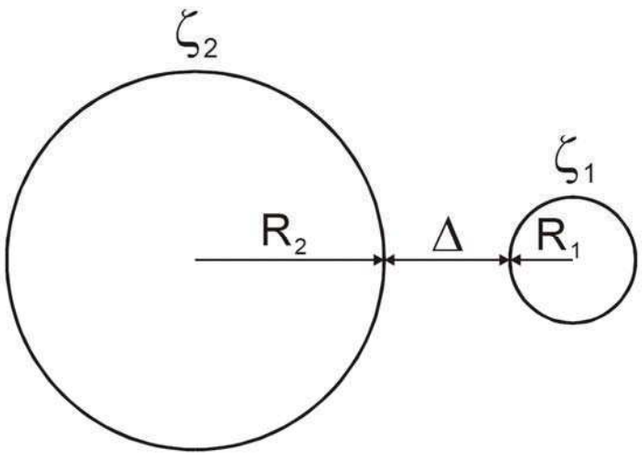


Fig. 10. Initial configuration of two circular vortices with parameters of separation distance, and two different radii and vorticity strengths. The small and strong vortex is the core.

Figure 10 illustrates the initial configuration of the binary vortex interaction for the concentric eyewall experiment, with relevant parameters of separation distance, radii and vorticity strength of the two vortices. Mallen et al. (2005) demonstrated that tropical cyclones are often characterized by a relatively slow decrease of tangential wind outside the radius of maximum wind, and hence by a a corresponding cyclonic vorticity skirt. The vorticity skirt can be easily incorporated into the binary vortex experiments. We consider an experiment with core vortex 7 times stronger in vorticity strength, and radius 4 times smaller in size than the neighboring large and weak vortex. The separation distance is 5 times the core radius and a vorticity skirt is also added to the core vortex outside the radius of maximum wind. Figure 11 gives the vorticity fields for such an experiment at hours 0, 6, and 12. By t = 6 h, Fig. 11 indicates the thin vorticity filaments have been wound several times, and by t = 12 h, vorticity mixing has created a halo of vorticity around the core vortex. Such a structure at t = 12 h is similar to the concentric eyewalls in the tropical cyclone. Noted that if such an event were to occur in a real tropical cyclone, and if it were observed by only a few radial legs of research aircraft,

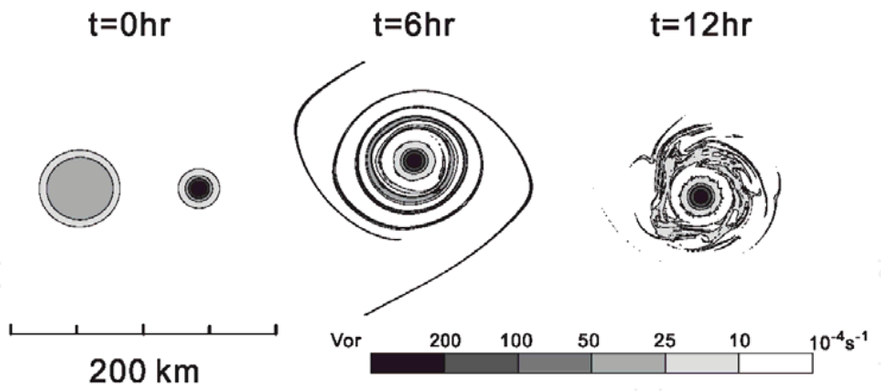


Fig. 11. Vorticity fields at t = 0, 6, and 12 h for an experiment with core vorticity 7 times stronger, size radius 4 times smaller than the large and small vortex nearby. The separation distance is 5 times the core radius. A vorticity skirt is also added to the core vortex outside the radius of maximum wind.

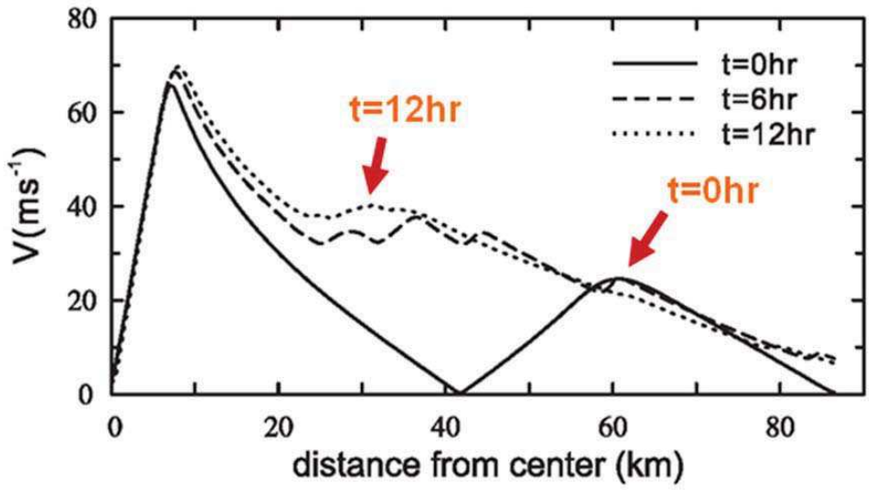


Fig. 12. The same as Fig. 10 except the tangential wind speed along a radial emanating westward from the center of the strong core vortex.

the asymmetric nature of the early revolution maybe lost. Figure 12 shows the tangential wind speed along a radial leg emanating westward from the center of the core vortex. The wind profiles show a secondary wind maximum that apparently contract s over a period of 12 h. During the contracting period, the secondary wind maximum increases from 25 m s^{-1} at 60 km to 40 m s^{-1} at 35 km. The features of the contraction are in general agreement with the observations of Hurricane Gilbert (Black & Willoughby, 1992). While the outer band contracting dynamics is often argued to be an axisymmetric gradient-balanced process involving advection by the divergent part of the flow (Shapiro & Willoughby, 1982), Fig. 12 suggests that vorticity advection by the nondivergent part of the flow can also contribute to the contraction dynamics in the concentric eyewalls formation.

In summary, we present observations indicating area of asymmetric convection outside the core vortex that wraps around the inner eyewall to form the concentric eyewalls in about 12 h. The observation suggests that an important element of concentric eyewalls formation maybe

the development of the symmetric structure from asymmetric convection. The dynamics are studied with an idealization of the interaction of a tropical cyclone core with nearby weaker vorticity with nondivergent bartropic dynamics. The results suggest that the contraction of the secondary wind maximum maybe a feature of vorticity dynamics. Kuo et al. (2004) suggests the pivotal role of the vorticity strength of the core vortex in maintaining itself, and in strectching, organizing and stabilizing the outer vorticity field, and the shielding effect of the moat to prevent further merger and enstrophy cascade processes in concentric eyewall dynamics. Kuo et al. (2008) further suggests that double eyewall of different sizes maybe explained by the binary vortex interaction with skirted parameter. The result also suggests that vorticity generation in the core and in the environment (via mesoscale convection) are of great importance in double eyewall dynamics. The vorticity dynamics of concentric eyewalls also serve as a nice example of the two-dimensional turbulence theory with the selective decay principle (McWilliams, 1984). The strong differential rotation outside the core vortex may yield straining out effect and produces vorticity filaments. With microwave satellite data, Kuo et al. (2009) found that the filamentation process tends to make an important contribution to the organization of the moat in strong typhoons with maximum wind greater than 130 kts. Filamentation effects are important for the convection process in TC environment, and likely relevant to the organization of convection, asymmetric structure, and moat formation. Since filamentation increases with increasing TC intensity, it plays a limitation role in convection particularly in the outer spiral band region. While the barotropic dynamics fall well short of a complete theory because of its neglect of vertical motion, the frictional boundary layer and diabatic process, the idealization gives significant insight to the organization and axisymmetrization aspects of concentric eyewalls structures.

4. Conclusion

In this chapter, we have reviewed important barotropic aspects of hurricane structure and intensity variability. First the dynamical model which governs divergent barotropic motions on an f-plane was introduced, and the fundamental dynamical properties were described. The important wave motions (vortex Rossby waves and inertia-gravity waves) of a linearized set of equations governing perturbations on an arbitrary axisymmetric vortex were described. The linear solutions were used to illustrate some barotropic aspects of observed spiral bands in hurricanes. Spiral rainbands close to the eyewall (or inner spiral rainbands), were shown to be most often sheared vortex Rossby waves, while the outer spiral bands that form away from the vortex basic state PV gradient can often be from a different mechanism. They could be inertia-gravity waves generated by flow imbalances from diabatic effects in the inner-core or generated spontaneously by the vortical motion in the hurricane core, or formed during the formative stages of the tropical cyclone via dynamic instability of larger-scale flow features, such as the inter-tropical convergence zone.

The barotropic model was next used to examine eyewall processes: barotropic instability of the hurricane eyewall and the ensuing PV and passive tracer mixing process between the eyewall and the eye. A conceptual model was described to illustrate the interaction of counter-propagating vortex Rossby waves. Numerical simulations of an unstable PV ring were then conducted to understand details of the mixing process. The numerical simulation exhibited polyonal eyewalls with straight line segments in the early part of the mixing process, and then the initially axisymmetric ring slowly symmetrized into a monopole. Observed polygonal eyewall shapes and eye swirls and mesovortices are believed to be evidence of this quasi-barotropic process occuring in hurricanes.

Finally, the dynamical model and observations was used to examine barotropic aspects of concentric eyewall cycles. Observations indicate that concentric eyewalls may form in asymmetric fashion as a result of the interaction of the vortex core with a weaker vorticity anomaly generated by convection. Due the deformation flow outside the vortex core, the outer weaker vorticity anomaly is strained out and elongated during the axisymmetrization process producing a secondary ring of enhanced vorticity. During this process the secondary wind maximum contracts, consistent with observations and full-physics numerical model simulations, indicating that a portion of concentric eyewall dynamics may be explained by potential vorticity advection.

In conclusion, we note that the divergent barotropic framework here is an oversimplification of the real atmosphere. In addition to neglecting vertical variations, we have also used a quasi-conservative framework without the effects of surface friction and diabatic heating. Both of these processes are elemental to hurricanes, and they create the secondary circulation responsible for intensification. Nonetheless, these results provide some fundamental asymmetric dynamics governing hurricane structure and intensity variability, in the absence of these factors.

5. Acknowledgements

We are grateful to Prof. Wayne Schubert and Dr. Scott Fulton for their comments and assistance. This research was performed in part while the first author held a National Research Council Research Associateship Award at the U.S. Naval Research Laboratory in Monterey, CA.

6. References

Andrews, D. G. (1983). A finite-amplitude Eliassen-Palm theorem in isentropic coordinates, *J. Atmos. Sci.* 40: 1877–1883.

Andrews, D. G., Holton, J. R. & Leovy, C. B. (1987). Middle atmosphere dynamics, *Academic Press.* p. 489 pages.

Barnes, G. M., Zipser, E. J., Jorgensen, D. & Marks, F., Jr. (1983). Mesoscale and convective structure of a rainband, *J. Atmos. Sci.* 40: 2125–2137.

Black, M. L. & Willoughby, H. E. (1992). The concentric eyewall cycle of Hurricane Gilbert, *Mon. Wea. Rev.* 120: 947–957.

Carr, L. E. & Williams, R. T. (1989). Barotropic vortex stability to perturbations from axisymmetry, *J. Atmos. Sci.* 46: 3177–3191.

Chen, Y. & Yau, M. K. (2001). Spiral bands in a simulated hurricane. part 1: Vortex Rossby wave verification, *J. Atmos. Sci.* 58: 2128–2145.

Cram, T. A., Persing, J., Montgomery, M. T. & Braun, S. A. (2007). A Lagrangian trajectory view on transport and mixing processes between the eye, eyewall, and environment using a high-resolution simulation of Hurricane Bonnie (1998), *J. Atmos. Sci.* 64: 1835–1856.

Dritschel, D. D. & Waugh, D. W. (1992). Quantification of the inelastic interaction of unequal vortices in two-dimensional vortex dynamics, *Phys. Fluids* 4: 1737–1744.

Eastin, M. D., Black, P. G. & Gray, W. M. (2002). Flight-level thermodynamic instrument wetting errors in hurricanes. Part I: Observations, *Mon. Wea. Rev.* 130: 825–841.

Ford, R. (1994). The instability of an axisymmetric vortex with monotonic potential vorticity in rotating shallow water, *J. Fluid Mech.* 280: 303–334.

Guinn, T. A. & Schubert, W. H. (1993). Hurricane spiral bands, *J. Atmos. Sci.* 50: 3380–3403.

Hendricks, E. A. & Schubert, W. H. (2009). Transport and mixing in idealized barotropic hurricane-like vortices, *Quart. J. Roy. Meteor. Soc.* 135: 1456–1470.

Hendricks, E. A. & Schubert, W. H. (2010). Adiabatic rearrangement of hollow PV towers, *J. Adv. Model. Earth. Sys.* Vol. 2, Art. #8, 19pp., doi:10.3894/JAMES.2010.2.8.

Hendricks, E. A., Schubert, W. H., McNoldy, B. D. & Fulton, S. R. (2010). Spontaneous-adjustment emission of inertia-gravity waves by unsteady vortical motion in the hurricane core, *Quart. J. Roy. Meteor. Soc.* 136: 537–548.

Hendricks, E. A., Schubert, W. H., Taft, R. K., Wang, H. & Kossin, J. P. (2009). Lifecycles of hurricane-like vorticity rings, *J. Atmos. Sci.* 66: 705–722.

Hodyss, D. & Nolan, D. S. (2008). The Rossby-inertia-buoyancy instability in baroclinic vortices, *Phys. Fluids* 20: 096602.

Kossin, J. P. & Eastin, M. D. (2001). Two distinct regimes in the kinematic and thermodynamic structure of the hurricane eye and eyewall, *J. Atmos. Sci.* 58: 1079–1090.

Kossin, J. P. & Schubert, W. H. (2001). Mesovortices, polygonal flow patterns, and rapid pressure falls in hurricane-like vortices, *J. Atmos. Sci.* 58: 2196–2209.

Kuo, H. C., Chang, C. P., Yang, Y. T. & Jiang, H.-J. (2009). Western North Pacific typhoons with concentric eyewalls, *Mon. Wea. Rev.* 137: 3758–3770.

Kuo, H.-C., Chen, G. T.-J. & Lin, C.-H. (2000). Merger of tropical cyclones Zeb and Alex, *Mon. Wea. Rev.* 128: 2967–2975.

Kuo, H. C., Lin, L.-Y., Chang, C.-P. & Williams, R. T. (2004). The formation of concentric vorticity structures in typhoons, *J. Atmos. Sci.* 61: 2722–2734.

Kuo, H. C., Schubert, W. H., Tsai, C. L. & Kuo, Y. F. (2008). Vortex interactions and barotropic aspects of concentric eyewall formation, *Mon. Wea. Rev.* 136: 5183–5198.

Kuo, H.-C., Williams, R. T. & Chen, J.-H. (1999). A possible mechanism for the eye rotation of Typhoon Herb, *J. Atmos. Sci.* 56: 1656–1673.

Kurihara, Y. M. (1979). On the development of spiral bands in tropical cyclones, *J. Atmos. Sci.* 33: 940–958.

Lander, M. A. & Holland, G. (1993). On the interaction of tropical-cyclone-scale vortices. I: Observations, *Quart. J. Roy. Meteor. Soc.* 119: 1347–1361.

Larson, R. N. (1975). Picture of the month–hurricane twins over the eastern North Pacific ocean, *Mon. Wea. Rev.* 103: 262–265.

MacDonald, N. J. (1968). The evidence for the existence of rossby-type waves on the hurricane vortex, *Tellus* 20: 138–150.

Mallen, K. J., Montgomery, M. T. & Wang, B. (2005). Reexamining the near-core radial structure fo the tropical cyclone primary circulation: Implications for vortex resiliency, *J. Atmos. Sci.* 62: 408–425.

McWilliams, J. C. (1984). The emergence of isolated, coherent vortices in turbulent flow, *J. Fluid Mech.* 46: 21–43.

Möller, J. D. & Montgomery, M. T. (2000). Tropical cyclone evolution via potential vorticity anomalies in a three-dimensional balance model, *J. Atmos. Sci.* 57: 3366–3387.

Möller, J. D. & Smith, R. K. (1994). The development of potential vorticity in a hurricane-like vortex, *Quart. J. Roy. Meteor. Soc.* 120: 1255–1265.

Montgomery, M. T., Bell, M. M., Aberson, S. D. & Black, M. L. (2006). Hurricane Isabel (2003). New insights into the physics of intense storms. Part I: Mean vortex structure and maximum intensity estimates, *Bull. Amer. Meteor. Soc.* 87: 1335–1347.

Montgomery, M. T. & Enagonio, J. (1998). Tropical cyclogensis via convectively forced vortex Rossby waves in a three-dimensional quasigeostrophic model, *J. Atmos. Sci.* 55: 3176–3207.

Montgomery, M. T. & Kallenbach, R. J. (1997). A theory for vortex Rossby waves and its application to spiral bands and intensity changes in hurricanes, *Quart. J. Roy. Meteor. Soc.* 123: 435–465.

Nakamura, N. (1996). Two-dimensional mixing, edge formation, and permeability diagnosed in area coordinates, *J. Atmos. Sci.* 53: 1524–1537.

Peng, J., Li, T., Peng, M. S. & Ge, X. (2008). Barotropic instability in the tropical cyclone outer region, *Quart. J. Roy. Meteor. Soc.* 135: 851–864.

Persing, J. & Montgomery, M. T. (2003). Hurricane superintensity, *J. Atmos. Sci.* 60: 2349–2371.

Prieto, R., McNoldy, B. D., Fulton, S. R. & Schubert, W. H. (2003). A classification of binary tropical cyclone-like vortex interactions, *Mon. Wea. Rev.* 131: 2656–2666.

Reasor, P. D., Montgomery, M. T., Marks, F. D. & Gamache, J. F. (2000). Low-wavenumber structure and evolution of the hurricane inner core observed by airborne dual-doppler radar, *Mon. Wea. Rev.* 128: 1653–1680.

Rozoff, C. M., Kossin, J. P., Schubert, W. H. & Mulero, P. J. (2009). Internal control of hurricane intensity: The dual nature of potential vorticity mixing., *J. Atmos. Sci.* 66: 133–147.

Rozoff, C. M., Schubert, W. H., McNoldy, B. D. & Kossin, J. P. (2006). Rapid filamentation zones in intense tropical cyclones, *J. Atmos. Sci.* 63: 325–340.

Schecter, D. A. & Montgomery, M. T. (2004). Damping and pumping of a vortex rossby wave in a monotonic cyclone: Critical layer stirring versus inertia-buoyancy wave emission, *Phys. Fluids* 16: 1334–1348.

Schubert, W. H., Montgomery, M. T., Taft, R. K., Guinn, T. A., Fulton, S. R., Kossin, J. P. & Edwards, J. P. (1999). Polygonal eyewalls, asymmetric eye contraction, and potential vorticity mixing in hurricanes, *J. Atmos. Sci.* 56: 1197–1223.

Shapiro, L. J. & Willoughby, H. E. (1982). The response of balanced hurricanes to local sources of heat and momentum, *J. Atmos. Sci.* 39: 378–394.

Wang, Y. (2002a). Vortex Rossby waves in a numerically simulated tropical cyclone. Part I: Overall structure, potential vorticity, and kinetic energy budgets, *J. Atmos. Sci.* 59: 1213–1238.

Wang, Y. (2002b). Vortex Rossby waves in a numerically simulated tropical cyclone. Part II: The role in tropical cyclone structure and intensity changes, *J. Atmos. Sci.* 59: 1239–1262.

Willoughby, H. E. (1978). A possible mechanism for the formation of hurricane rainbands, *J. Atmos. Sci.* 35: 838–848.



Recent Hurricane Research - Climate, Dynamics, and Societal Impacts

Edited by Prof. Anthony Lupo

ISBN 978-953-307-238-8
Hard cover, 616 pages
Publisher InTech
Published online 19, April, 2011
Published in print edition April, 2011

This book represents recent research on tropical cyclones and their impact, and a wide range of topics are covered. An updated global climatology is presented, including the global occurrence of tropical cyclones and the terrestrial factors that may contribute to the variability and long-term trends in their occurrence. Research also examines long term trends in tropical cyclone occurrences and intensity as related to solar activity, while other research discusses the impact climate change may have on these storms. The dynamics and structure of tropical cyclones are studied, with traditional diagnostics employed to examine these as well as more modern approaches in examining their thermodynamics. The book aptly demonstrates how new research into short-range forecasting of tropical cyclone tracks and intensities using satellite information has led to significant improvements. In looking at societal and ecological risks, and damage assessment, authors investigate the use of technology for anticipating, and later evaluating, the amount of damage that is done to human society, watersheds, and forests by land-falling storms. The economic and ecological vulnerability of coastal regions are also studied and are supported by case studies which examine the potential hazards related to the evacuation of populated areas, including medical facilities. These studies provide decision makers with a potential basis for developing improved evacuation techniques.

How to reference

In order to correctly reference this scholarly work, feel free to copy and paste the following:

Eric A. Hendricks, Hung-Chi Kuo, Melinda S. Peng and Daniel Hodyss (2011). Barotropic Aspects of Hurricane Structural and Intensity Variability, Recent Hurricane Research - Climate, Dynamics, and Societal Impacts, Prof. Anthony Lupo (Ed.), ISBN: 978-953-307-238-8, InTech, Available from: http://www.intechopen.com/books/recent-hurricane-research-climate-dynamics-and-societal-impacts/barotropic-aspects-of-hurricane-structural-and-intensity-variability

INTECH
open science | open minds

InTech Europe
University Campus STeP Ri
Slavka Krautzeka 83/A
51000 Rijeka, Croatia
Phone: +385 (51) 770 447
Fax: +385 (51) 686 166

InTech China
Unit 405, Office Block, Hotel Equatorial Shanghai
No.65, Yan An Road (West), Shanghai, 200040, China
中国上海市延安西路65号上海国际贵都大饭店办公楼405单元
Phone: +86-21-62489820
Fax: +86-21-62489821

www.intechopen.com

IntechOpen

IntechOpen

© 2011 The Author(s). Licensee IntechOpen. This chapter is distributed under the terms of the Creative Commons Attribution-NonCommercial-ShareAlike-3.0 License, which permits use, distribution and reproduction for non-commercial purposes, provided the original is properly cited and derivative works building on this content are distributed under the same license.

IntechOpen

IntechOpen